Tunable surface morphology via patterned cavities in soft materials

Xiangbiao Liao,[1,*] Takumi Nagakura,[1,2,*] Youlong Chen,[1,3] Liangliang Zhu,[4] Xiaoyang Shi,[1] Akio Yonezu,[1,2] Xi Chen,[1,4] and Hang Xiao[1,4,†]

[1]*Yonghong Zhang Family Center for Advanced Materials for Energy and Environment, Department of Earth and Environmental Engineering, Columbia University, New York, New York 10027, USA*

[2]*Department of Precision Mechanics, Chuo University, 1-13-27 Kasuga, Bunkyo, Tokyo 112-8551, Japan*

[3]*International Center for Applied Mechanics, SV Laboratory, School of Aerospace, Xi'an Jiaotong University, Xi'an 710049, China*

[4]*School of Chemical Engineering, Northwest University, Xi'an 710069, China*

(Received 19 September 2018; published 17 December 2018)

There is a rich diversity of surface topologies controllably engineered by patterning cavities embedded beneath the surface of soft materials. Upon external compression, the surface undergoes the reversible transformation from the flat surface to various surface topographies, including a periodic checkerboard pattern with alternate convex and concave features. To design the surface features, both two- (2D) and three-dimensional (3D) finite element based simulations are performed. It is demonstrated that the periodic surface features with controllable morphology, such as one-dimensional waves, checkerboard pattern, and mutually perpendicular apexes, etc., can be realized through varying cavity geometries (e.g., relative intercavity distance, shapes, and biaxial or uniaxial load). Additionally, a simple model for plate buckling is used to elucidate the effect of cavity aspect ratio on the surface pattern. Based on 3D printed prototypes, we further conduct experiments to validate the simulation results of 2D morphologies. The patterned cavities in soft materials make designing a variety of reversible surface features possible, offering an effective fabrication approach for wide application across multiple scales.

DOI: 10.1103/PhysRevE.98.063004

I. INTRODUCTION

Surface features play a significant role in the behaviors of natural and biological systems [1–3]. For example, folds in the brain help enhance intellectual capacity and furrows grow on plant surfaces during the aging process. In engineering systems, various methods have been developed to engineer such surface topologies, including periodic wrinkles, random bumps, and local creases. It has also been shown that the reversibility of these features allows not only extensive applications in optics [4] and flexible electronics [5], but also in tuning the properties of surface adhesion [6] and hydrophobicity [7], etc. Recent studies have focused on the stressed layered systems and the sinusoidal pattern of wrinkles [1]. More fascinating wrinkling patterns including stripes, herringbones, zigzag labyrinths [8,9], and buckyballlike features are obtained by tuning anisotropic stress in bilayers [10–12]. Beyond wrinkles, a variety of surface localizations, including folding [13,14], ridging, and delaminated buckling, were also observed [3,15–17].

Defects (for example, voids, rigid elements) have traditionally been regarded as imperfections that affect the formation of surface wrinkles or localizations [18,19]. Conversely, researchers have recently utilized the prepatterned holes and rigid particles to produce new intriguing surface features in bilayers [20,21]. In addition, the composite of soft material with embedded particles was studied to allow the controllability of surface topographies [22]. While this study benefits many applications, the features are local. Despite extensive works on engineering the surface of composite systems, limited studies focus on homogeneous materials.

Here, we focus on the cavity-embedded soft materials (CESMs) with prepatterned cavities below the surface. The design of cavity patterns opens an avenue to exploit periodic surface features in homogeneous materials under external in-plane compression. Through finite element calculations, the surface morphology is found to be controllable by the shape and spacing of intercavities when the soft materials are subjected to external stimuli. Our parallel experiments based on 3D-printed prototypes consolidate the simulation results. Thus, this method enables the reversibility and continuity of surface changes and is applicable for structures and materials across multiple length scales.

Numerical model. Both the two- (2D) and three-dimensional (3D) nonlinear numerical simulations were performed through the commercial software ABAQUS to investigate the changes of surface features. The CESMs were modeled as a nearly incompressible material using neo-Hookean constitution, which has initial shear modulus $G = 0.50$ MPa corresponding to the commercial rubber (TangoPlus) used in the experiments. Periodic boundary conditions were applied to the lateral sides. Neither vertical displacement nor shear traction was allowed on the bottom surface.

II. EXPERIMENTAL METHODS

The physical prototypes were fabricated by an Objet500 Connex 3D printer. The prototypes were made of

*These authors contributed equally to this work.
†hx2152@columbia.edu

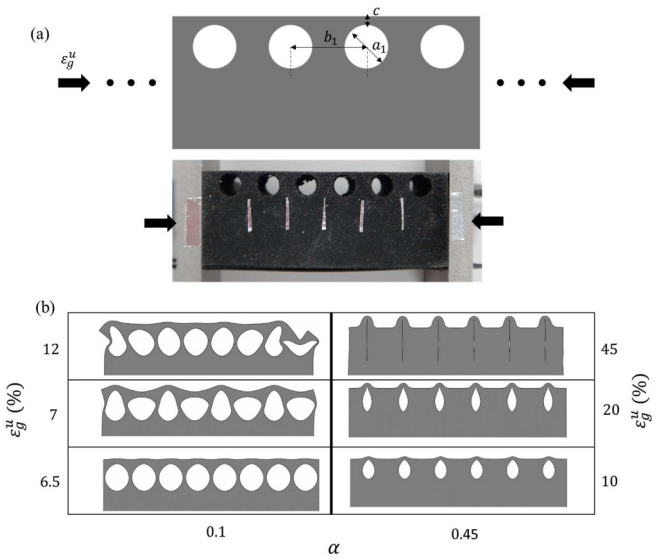

FIG. 1. (a) The top figure: a representative segment of a CESM under a global compressive strain and with labeled geometrical dimensions; the bottom figure: the experimental setup of uniaxial compressing of the 3D printed material. (b) The phase diagram of simulated surface textures with respect to the uniaxial compressive strain and value of α, while β is set to be 0.2.

photosensitive polymeric materials, TangoPlus. We conducted the uniaxial compression tests with a ZwickRoell Z2.5 mechanical tester. To ensure plane strain conditions in the compressive test, the samples were sandwiched between two optically clear acrylic plates and another plate was placed below the samples. The friction between the plates and the sample was reduced by using mineral oil. Twenty percent global compressive strain was applied to each sample with a strain rate of 0.0005 s^{-1}. A high resolution camera was placed in front of the sample and took a picture every minute.

III. RESULTS AND DISCUSSIONS

A. 2D modeling

We start from the 2D representative segment of CESMs shown in Fig. 1(a). Underneath the top surfaces, there is one row of circular cavities with diameter a_1, intercavity spacing b_1 and depth c. We construct the dimensionless parameters: relative intercavity spacing $\alpha = \frac{b_1 - a_1}{a_1}$, relative distance from the surface $\beta = \frac{c}{a_1}$. When subjected to increasing uniaxial global compression ε_g^u, two representative CESMs with different intercavity distances show different morphological evolutions, with the phase diagram illustrated in Fig. 1(b). When the relative intercavity distance is small, for example, $\alpha = 0.1$, the initially flat surface transits from local bumps to periodic waves with the wavelength of doubling cavity spacing, followed by one cavity collapsing. Upon the global strain reaching 6.8%, the array of cavities suddenly transforms into a periodic pattern of alternating, mutually orthogonal ones. This buckling mechanism should be responsible for the periodic surface feature and the cavity collapsing release under further compression. However, because the interaction between adjacent cavities in the CESMs with larger intercavity distance ($\alpha = 0.45$) is small, only local ridges right above the cavities are formed. Further compression (up to 45%) induces the closing of the cavity and the high amplitude-to-wavelength ratio ridges, which allows the application in superhydrophobic coatings. The amplitude is half of the distance between the peak and the valley in the surface buckling texture, and the wavelength is the closest distance between peaks. Furthermore, the transition value of relative intercavity spacing, $\alpha = 0.25$, can differentiate the two deformation mechanisms.

To validate the simulation results, we fabricated the cavity-embedded substrate samples using 3D printing and compressed them by only 25% global strain to avoid global buckling of samples, illustrated in the bottom of Fig. 1(a). The images of surface patterns for both $\alpha = 0.1$ and $\alpha = 0.45$ were captured by a camera. As shown in Fig. 2(a), the morphological evolutions for these two samples undergoing increasing compression are qualitatively consistent with those simulation results in Fig. 1(b). Quantitatively, the critical global strain for intercavity instability in the experiment is 6.0% for $\alpha = 0.1$, which matches well with the simulated value of 6.8% above. The small deviation may be attributed to the nonperiodic boundary conditions at the compressor heads and the dynamic effect induced by the relatively high loading rate. Furthermore, we plot the experimental and simulated results of the amplitude-to-wavelength ratio for $\alpha = 0.45$ as

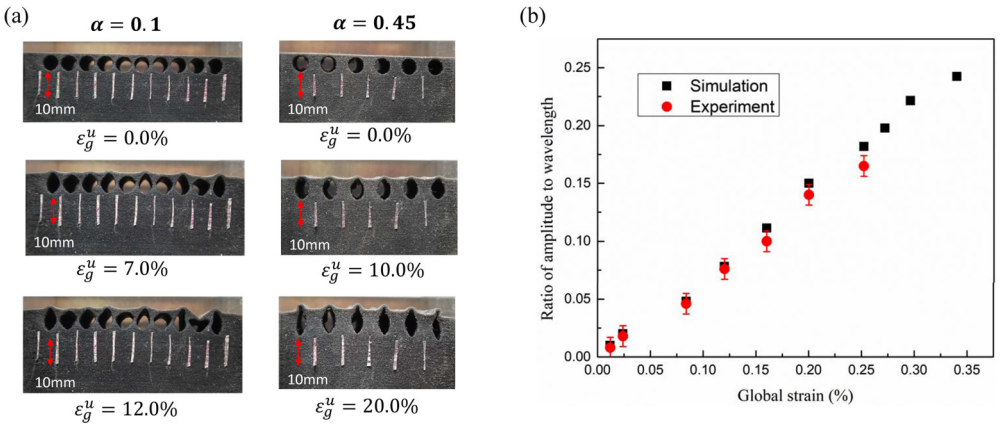

FIG. 2. (a) Experimental surface evolutions of 3D-printed CESM prototypes with different values of α, while β is set to be 0.2. (b) The comparison of amplitude-wavelength ratio between the simulation and experiment for $\alpha = 0.45$.

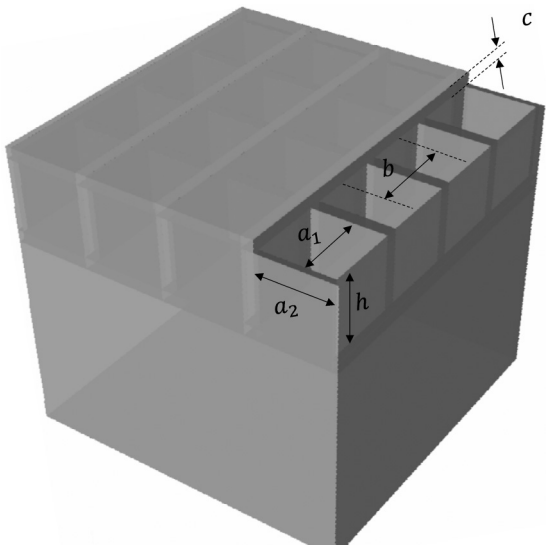

FIG. 3. Schematics of representative CESMs with patterned cuboidal cavities. The characteristic geometrical dimensions are labeled.

the global strain increasing in Fig. 2(b), indicating quantitative agreement between the experiment and simulation. Therefore, the controllability of surface morphologies through varying global strain and geometrical parameters offers an alternative strategy to reversibly and repeatedly switch surface topography by involving embedded cavities within a soft material.

B. 3D modeling

To investigate more fascinating surface patterns in soft materials, 3D cavities with different shapes are introduced underneath the material surfaces. The exemplary 3D segment of CESM shown in Fig. 3 includes cuboidal cavities. Note that other geometries for cavity can also be embedded, for example, spherical cavities. We construct the dimensionless parameters: relative intercavity spacing $\alpha_i = \frac{b_i - a_i}{a_i}$ $(i = 1,\ 2)$, relative distance from the surface $\beta = \frac{c}{a_2}$, and aspect ratio $\gamma = \frac{a_1}{a_2}$, to study the effect of cavity geometry on surface features. Based on the finite element simulation, the morphological evolutions of 3D CESMs undergoing either uniaxial ε_g^u or biaxial compressive strain ε_g^b are studied.

Figure 4(a) shows the diagram of cross sections of CESMs with cuboidal cavity patterns with respect to the uniaxial compressive strain and the geometrical parameter γ. In the case of $\gamma = 1$, the surface stays flat until the critical compressive strain reaches 5.5%, and then the checkerboard pattern is triggered by the mechanical buckling, forming the alternate concave and convex feature shown in Fig. 4(b). The compressive strain in the plates is released by out-of-plane bending deformation; further compression still maintains this topology but increases the amplitude. As shown in the side views of deformed CESMs in Fig. 4(a), the instability-induced transformation of the original cavity geometry should be responsible for the checkerboard pattern with the wavelength of $2a_1$. However, for the cavities with aspect ratio $\gamma = 2$, the high-order checkerboard pattern with the wavelength of a_1 occurs first at the critical strain of 7.2% shown in Fig. 4(a). At 14%, two checkerboard surface textures with different wavelengths are demonstrated in Fig. 4(c).

To address the effect of aspect ratio on surface pattern, we adopt a simple stability analysis. A plate with lateral periodicity (the thickness of t, length of a_1, and width of a_2), right above the cavities, is adopted for analysis and subjected to uniaxial compression in the a_1 direction. The critical membrane force in the length direction for buckling is calculated as $N_{xcr} = \frac{\pi^2 D}{a_1^2}(m + \frac{1}{m}\frac{a_1^2}{a_2^2})^2$, where D is the bending

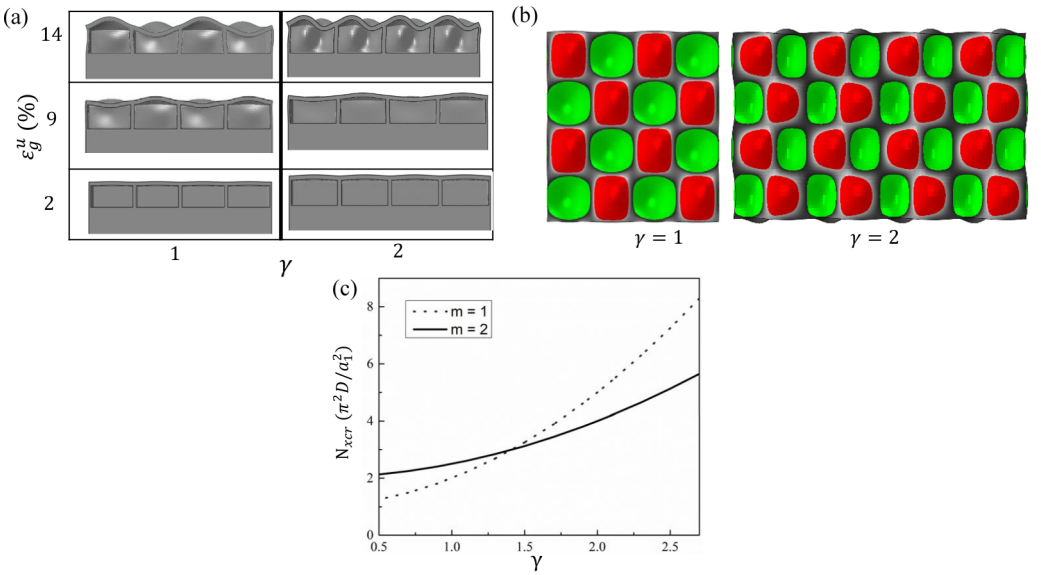

FIG. 4. (a) The phase diagram of simulated surface textures (cross sections) with respective to the uniaxial compressive strain and value of γ, while β is set to be 0.2 in the cuboidal cavity-embedded CESMs. (b) The surface morphologies of cuboidal cavity-embedded CESMs for $\gamma = 1$ and $\gamma = 2$ at the uniaxial global compression of 14%. (c) Theoretically critical membrane forces of plates for different buckling modes m as a function of the aspect ratio γ of cuboidal cavity.

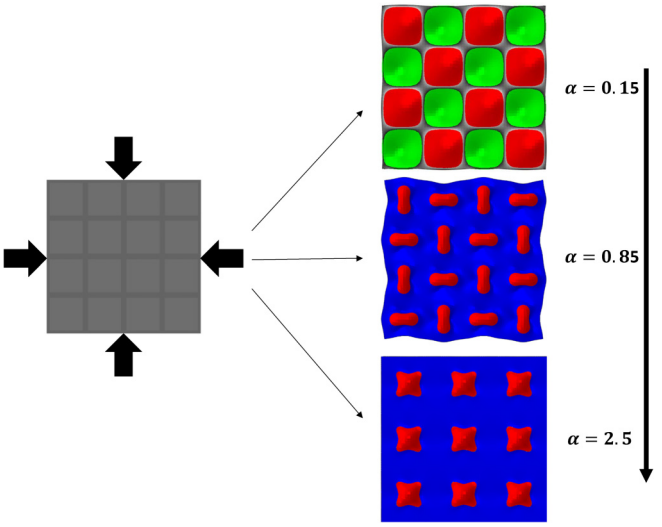

FIG. 5. The surface morphologies of cuboidal cavity-embedded CESMs with α undergoing the same biaxial global compression of 12%.

stiffness of the plate and m refers to the number of half wavelengths of the buckling plate [23]. The relation of N_{xcr} with a_1/a_2 is plotted in Fig. 4(c) for different values of m. It is illustrated that the critical force for $m = 1$ is smaller than that for $m = 2$ in the case of $\frac{a_1}{a_2} = 1$, which explains the preference of the checkerboard pattern with wavelength of $2a_1$ as applying uniaxial compression in our simulation. However, the buckling mode of $m = 2$, corresponding to the wavelength of a_1, is illustrated to occur preferably when the aspect ratio is 2. It is consistent with our simulation result shown in Fig. 4(a). Although vertical walls in between cavities are not considered in this model, the qualitative agreement with the simulation results emphasizes the significance of cavity aspect ratio on buckling patterns.

Besides the aspect ratio, other parameters of the cavity can be used to switch the surface topologies, including loading strategies and cavity shapes, etc. Figure 5 shows the surface patterns of CESMs at 12% biaxial compressive strain for values of $\alpha = 0.15$, 0.85, and 2.5, and all cavities are kept cuboidal. With increasing relative intercavity spacing, the surface topology varies from checkerboard pattern to alternating mutually orthogonal peanuts, followed by local features: quadrangular bumps. The mechanism changes from buckling-induced intercavity instability to local deformation due to weaker interaction between cavities in the case of larger α value.

We further study the effect of cavity shape and row number on the topological evolution of CESMs under different loading conditions: uniaxial and biaxial compression. The intercavity spacing, relative distance from the surface, and aspect ratio are set to be constant for all cases. Figure 6(a) presents the results of surface topology for a spherical cavity with a square lattice and biaxial global compression, and shows the square array of convex bump transforms into alternating mutually orthogonal peanuts when the global compressive strain increases from 13% to 16%. However, the surface patterns with larger bumps followed by alternating mutually orthogonal ellipses are observed when we initially introduce hemispherical cavities, which are demonstrated in Fig. 6(b). This difference is mainly due to the center of hemispherical cavity being closer to the top surface compared to the spherical cavity scenario when the value of β is the same. Furthermore, the row number can be used to change the surface topography. We arrange a single row of cavities in line with the loading direction. The surface morphology in Fig. 6(c) is similar to those in Fig. 6(a) for the square array of spherical cavities, but the hemispherical cavities induce a nonsymmetric surface pattern at the global strain of 24% in Fig. 6(d), which is very different from the square array of hemispherical cavities under biaxial compression. This transition from a symmetric into a nonsymmetric surface is caused by the instability of the cavities underneath. It is found that the instability occurs upon reaching a critical compressive strain. Although our results demonstrate that a single row of cavities is able to trigger the symmetric to nonsymmetric surface morphology transition, there are other potentially important parameters for tuning the

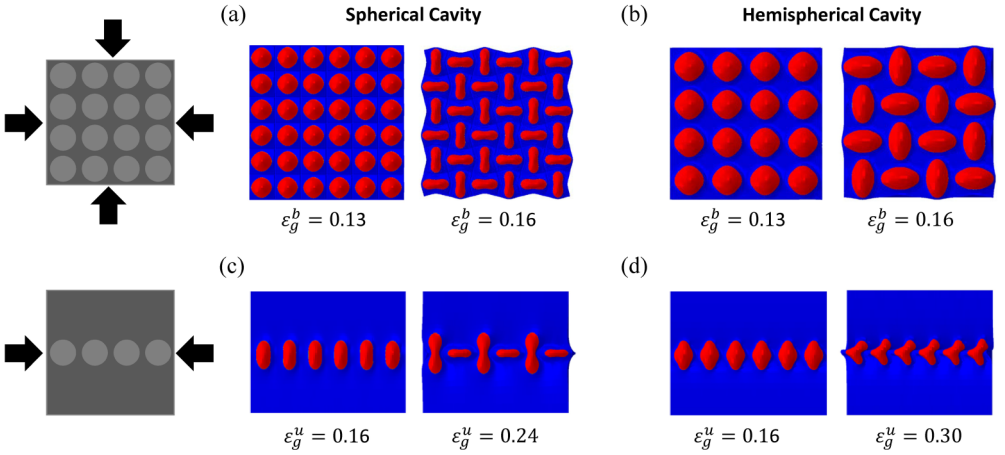

FIG. 6. The surface morphologies of CESMs with square patterns of (a) spherical and (b) hemispherical cavities undergoing different biaxial global compression. The surface morphologies of CESMs with one column of (c) spherical and (d) hemispherical cavities undergoing different uniaxial global compression.

surface morphology, including heterogeneous shapes, mixture of cavity and hard particles, and cavity patterns, which will be subjected to further study.

IV. CONCLUSION

In this study, a series of 2D and 3D surface topographies are created in soft materials with an embedded cavity array. Both simulation and experimental efforts confirm that by varying the geometries of cavities (sizes, shapes, arrays) and loading methods (uniaxial and biaxial compression), we can dynamically tune the surface evolutions. The variety of overall and local morphologies is revealed to be based on the intercavity instability and local deformation of top plates, respectively. The flexibility provided by CESMs underpins a novel design of tunable surface patterns that can be applied to multiscale applications. The tunable surface topography allows optimization of chemical and physical properties in real applications which need dynamically controllable surfaces.

ACKNOWLEDGMENTS

X.C. acknowledges the support from the National Natural Science Foundation of China (Grants No. 11172231 and No. 11372241), ARPA-E (Grant No. DE-AR0000396) and AFOSR (Grant No. FA9550-12-1-0159); the work is supported by Yonghong Zhang Family Center for Advanced Materials for Energy and Environment; X.L., L.Z., and H.X. acknowledge the China Scholarship Council for the financial support.

[1] N. Bowden, S. Brittain, A. G. Evans, J. W. Hutchinson, and G. M. Whitesides, Nature **393**, 146 (1998).
[2] X. Chen and J. Yin, Soft Matter **6**, 5667 (2010).
[3] B. Li, Y.-P. Cao, X.-Q. Feng, and H. Gao, Soft Matter **8**, 5728 (2012).
[4] L. M. Mathger, E. J. Denton, N. J. Marshall, and R. T. Hanlon, J. R. Soc., Interface **6 Suppl. 2**, S149 (2009).
[5] D.-Y. Khang, H. Jiang, Y. Huang, and J. A. Rogers, Science **311**, 208 (2006).
[6] E. P. Chan, E. J. Smith, R. C. Hayward, and A. J. Crosby, Adv. Mater. **20**, 711 (2008).
[7] S. Yang, K. Khare, and P.-C. Lin, Adv. Funct. Mater. **20**, 2550 (2010).
[8] X. Chen and J. W. Hutchinson, Scr. Mater. **50**, 797 (2004).
[9] Z. Y. Huang, W. Hong, and Z. Suo, J. Mech. Phys. Solids **53**, 2101 (2005).
[10] B. Li, F. Jia, Y.-P. Cao, X.-Q. Feng, and H. Gao, Phys. Rev. Lett. **106**, 234301 (2011).
[11] J. Yin, Z. Cao, C. Li, I. Sheinman, and X. Chen, Proc. Natl. Acad. Sci. USA **105**, 19132 (2008).
[12] J. Yin, X. Chen, and I. Sheinman, J. Mech. Phys. Solids **57**, 1470 (2009).
[13] C. Cao, H. F. Chan, J. Zang, K. W. Leong, and X. Zhao, Adv. Mater. **26**, 1763 (2014).
[14] S. Singamaneni, M. E. McConney, and V. V. Tsukruk, Adv. Mater. **22**, 1263 (2010).
[15] J. B. Kim, P. Kim, N. C. Pégard, S. J. Oh, C. R. Kagan, J. W. Fleischer, H. A. Stone, and Y.-L. Loo, Nat. Photonics **6**, 327 (2012).
[16] F. Brau, P. Damman, H. Diamant, and T. A. Witten, Soft Matter **9**, 8177 (2013).
[17] B. J. Gurmessa and A. B. Croll, Soft Matter **13**, 1764 (2017).
[18] Y. Zhao, W. M. Huang, and Y. Q. Fu, J. Micromech. Microeng. **21**, 067007 (2011).
[19] H. Vandeparre, S. Gabriele, F. Brau, C. Gay, K. K. Parker, and P. Damman, Soft Matter **6**, 5751 (2010).
[20] J. T. Paci, C. T. Chapman, W. K. Lee, T. W. Odom, and G. C. Schatz, ACS Appl. Mater. Interfaces **9**, 9079 (2017).
[21] Y. Zheng, G.-Y. Li, Y. Cao, and X.-Q. Feng, Extreme Mech. Lett. **11**, 121 (2017).
[22] M. Guttag and M. C. Boyce, Adv. Funct. Mater. **25**, 3641 (2015).
[23] S. P. Timoshenko and J. M. Gere, *Theory of Elastic Stability* (McGraw Hill–Kogakusha Ltd., Tokyo, 1961), p. 109.